Advanced Electronic Materials

ADVANCED ELECTRONIC MATERIALS Open Access

www.advelectronicmat.de

RESEARCH ARTICLE OPEN ACCESS

Capacitive Pixelated CMOS Electronic Nose

M. A. Basyooni-M. Kabatas[1] | Tao Shen[2] | Kaï Betlem[1] | Chunyu Huang[3] | Monique A. van der Veen[3] | Frans Widdershoven[2,4] | Murali K. Ghatkesar[1] | Peter G. Steeneken[1]

[1]Department of Precision and Microsystems Engineering, Delft University of Technology, Delft, The Netherlands | [2]Department of Microelectronics, Delft University of Technology, Delft, The Netherlands | [3]Chemical Engineering Department, Delft University of Technology, Delft, The Netherlands | [4]NXP Semiconductors, Technology & Operations/CTO Office, Eindhoven, The Netherlands

Correspondence: M. A. Basyooni-M. Kabatas (m.kabatas@tudelft.nl) | Peter G. Steeneken (p.g.steeneken@tudelft.nl)

Received: 19 November 2025 | **Revised:** 11 March 2026 | **Accepted:** 10 April 2026

Keywords: capacitive gas sensor | electronic nose (E-nose) | metal–organic frameworks (MOFs) | volatile organic compounds (VOCs)

ABSTRACT

Although some of the human senses can nowadays be replaced by low-cost electronic sensors such as microphones and image sensors, a compact low-cost electronic nose (E-nose) remains elusive. In this work, an E-nose is presented that can capacitively detect volatile organic compounds (VOCs). The E-nose consists of an array of 1024 capacitive microelectrodes on a complementary metal-oxide-semiconductor (CMOS) chip, functionalized by inkjet printing. The pixels are coated with a UV-curable ink and metal–organic frameworks (MOFs: ZIF-8, MIL-101(Cr), MIL-140A) to create chemically diverse microdomains that generate gas-specific response patterns through adsorption-driven dielectric loading. ZIF-8 exhibits the highest response to 2-butanone, whereas the UV-curable layer responds most strongly to toluene; both show low cross-sensitivity to water vapor, enabling operation under humid conditions. After calibration in pure gases, reproducible responses to controlled binary mixtures of toluene and 2-butanone are observed. The device operates at low power, combines a large 1024-pixel array with CMOS integration, and offers application-specific functionalization by inkjet printing, providing both low cost and versatility. By further extending the range of functionalization materials, the E-nose can be applied to analyze a wide variety of gases, with potential applications in safety monitoring, health, agriculture, and robotics.

1 | Introduction

Identification of volatile organic compounds (VOCs) is important for food quality control, health monitoring, and pest management [1]. Various VOC detection techniques exist, including infrared (IR) spectrometers [2], laser absorption spectroscopy (LAS) [3], and gas chromatography coupled with mass spectrometry (GC-MS) [4]. However, these techniques require instruments that are not easily portable, consume substantial power, and are relatively expensive. Since many applications require detectors that can continuously monitor the gas composition in situ, for example in early pest management in agriculture, indoor air-quality monitoring, and food spoilage detection, there is a strong need to develop compact, low-cost electronic noses (E-noses).

Electronic noses combine arrays of broadly responsive chemical sensors with pattern-recognition algorithms to generate odour fingerprints that enable discrimination of complex VOC mixtures. They have been applied in diverse domains, including breath analysis for medical diagnostics and disease screening [5–7], environmental and indoor air-quality monitoring, food and beverage quality control, and industrial or safety-related VOC surveillance [8]. Recent work has also demonstrated robust chemical classification using advanced chemosensor platforms coupled with machine learning, for example graphene-based sensor arrays [9]. In these scenarios, E-noses complement analytical techniques such as GC-MS and spectroscopic methods, which remain the gold standard for detailed laboratory analysis but are less suited to compact, low-power, continuous field deployment.

Recent studies have set steps toward this goal by demonstrating real-time VOC detection with E-nose sensors that electronically detect gases via property changes in sensing materials, affecting capacitance [10–14], resistance [15], or luminescence [16] of dedicated functionalization materials, which are deposited between the electrodes of the E-nose sensor. Most of these works focus on a single or low number of sensing elements per chip. In the present work, we deliberately employ a capacitive transducer architecture rather than a resistive one. In our CMOS implementation [17], the metal electrodes are fully covered by a dielectric layer and are therefore not in direct contact with the sensing film. This configuration protects the electrodes from electrochemical attack and contamination, which improves the long-term stability and chemical robustness of the device. Moreover, the capacitive signal originates from adsorption-driven changes in the effective dielectric constant of the functional layer, without any DC current flowing directly through the sensing material. As a result, Joule heating and electrically induced degradation of the sensing film are avoided, leading to more stable and reproducible responses over many exposure cycles.

In typical E-nose concepts, individual vapor sensors are not designed as highly specific "lock-and-key" receptors for a single analyte. Instead, each sensor element is broadly responsive to a range of vapours and exhibits a characteristic response pattern across different analytes. By combining the parallel outputs of an array of such partially-specific sensors, an odour fingerprint is obtained that can be used to discriminate and quantify complex gas mixtures after appropriate training [18]. This principle was already demonstrated by Persaud and Dodd, who showed that a model electronic nose can reproducibly distinguish a wide variety of odors without requiring highly specific receptors [18]. Consequently, the role of a large sensor array is not to provide one unique sensor per gas, but to span a multidimensional response space in which different VOCs and mixtures map to separable patterns.

As sensing layers, we employ MOFs, a class of porous crystalline materials composed of metal nodes and organic linkers that can offer high surface areas, tunable pore structures, and chemical robustness, making them attractive for VOC sensing. In this work, we focus on three representative MOFs: ZIF-8, MIL-101(Cr), and MIL-140A. ZIF-8 is a zeolitic imidazolate framework with small hydrophobic cages and narrow windows; MIL-101(Cr) features large three-dimensional cages with coordinatively unsaturated metal sites; and MIL-140A is a one-dimensional channel system with ZrO backbones. These materials were selected because they combine distinct pore architectures and hydrophilicity with good thermal and water stability, allowing us to study how different MOF structures influence VOC adsorption and sensor response. The detailed structural and adsorption characteristics of these MOFs are summarized in the Supporting Information.

To realize such an E-nose with multiple sensor elements requires addressing two key challenges:

1. Realizing a large number of sensor elements that can be individually read out on a small area with low-cost electronics.
2. Providing multiple different functionalization materials in the sensor area.

Here, we present a pixelated capacitive CMOS electronic nose with on-chip readout and inkjet-printed MOF-based and polymer-based functional layers. After calibration in pure gases, the E-nose yields reproducible, gas-specific response patterns and supports concentration estimation for single-component exposures using linear or quadratic calibration models. Responses to binary gas mixtures are reported qualitatively.

2 | Experimental

2.1 | Nanoparticle Synthesis and Characterization

2.1.1 | Chemicals

Three types of metal–organic framework (MOF) nanoparticles were synthesized in powder form, of which ZIF-8 was found to be the most suitable, and was therefore used for the final E-Nose experiment. The synthesis of MOF nanoparticles was carried out using the following high-purity chemical reagents. Zinc nitrate hexahydrate (98%, Sigma–Aldrich) and 2-methylimidazole (98%, TCL) were used as precursors for ZIF-8 synthesis. For the preparation of MIL-140A, N,N-Dimethylformamide (DMF) (≥99.9%, Sigma–Aldrich), terephthalic acid (98%, Merck Sigma), and zirconium chloride (99.5%, Thermo Fisher Scientific) were employed. Chromium chloride hexahydrate (96%, Merck Sigma) and terephthalic acid (98%, Merck Sigma) were utilized for MIL-101(Cr) synthesis. Additionally, methanol (≥99.9%, Honeywell), and ethanol (99.5%, Thermo Fisher) were utilized in the respective synthesis processes. All aqueous solutions were prepared using ultrafiltrated deionized (DI) water with a resistivity of 18.0 Mcm, obtained from an LWTN Genie A system (Laboratorium Water Technologie Nederland).

2.1.2 | Synthesis of ZIF-8

ZIF-8 was synthesized following a previously reported method [19], with slight modifications. First, 1.17 g of $Zn(NO_3)_2{\cdot}6H_2O$ was dissolved in 8 mL of deionized (DI) water. Separately, 22.7 g of 2-methylimidazole was dissolved in 80 mL of DI water. The two precursor solutions were mixed and stirred at room temperature (22°C) for 5 min. The resulting product was observed to immediately become a milky suspension. The precipitate was collected by centrifugation, washed three times with methanol at 15 000 Relative Centrifugal Force (RCF) for 30 min, and finally dried in a vacuum oven at 65°C overnight.

2.1.3 | Synthesis of MIL-101(Cr)

MIL-101(Cr) was synthesized hydrothermally using 1.26 mmol of $CrCl_3{\cdot}6H_2O$ and 1.26 mmol of terephthalic acid. These compounds were combined in a 40 mL autoclave and dispersed in 20 mL of deionized (DI) water using 10 min of sonication. The autoclave was then sealed and placed in an oven at 180°C for 48 h. After cooling to room temperature (RT), the autoclave was opened, and the precipitate was manually stirred using a

disposable spatula to redisperse the particles. The product was transferred to 50 mL centrifuge tubes and centrifuged at 15 000 RCF for 30 min. The resulting supernatant was removed, and further washing was performed to eliminate residual reactants and unreacted precursors: the sample was resuspended in 30 mL of N,N-Dimethylformamide (DMF) using 10 min of sonication. The mixture was poured back into the autoclave, resealed, and heated at 60°C for 3 h. After cooling to RT, the mixture was transferred back into centrifuge tubes and centrifuged at 15 000 RCF for 30 min. This washing process was repeated twice with DMF and once with ethanol (EtOH) to ensure thorough purification. After the final washing step with ethanol, the residue was dried overnight in a vacuum oven at RT. The dried as-synthesized samples were weighed and collected in 5 mL glass sample vials. The final activation step was carried out by drying the powder in a vacuum oven at 150°C for 8 h under vacuum, ensuring complete removal of residual solvents and achieving full activation of the material.

2.1.4 | Synthesis of MIL-140A

MIL-140A was synthesized by dissolving 1.75 mmol of $ZrCl_4$ in 10 mL of DMF and 1.75 mmol of terephthalic acid in 10 mL of DMF. Both solutions were ultrasonicated for 20 min, then combined and sonicated for an additional 5 min. The resulting solution was transferred into a 40 mL PTFE-lined autoclave and heated at 140°C for 24 h. After synthesis, the product was washed three times with DMF. A solvent-exchange step was performed by soaking the powder in methanol for 24 h, after which the methanol was discarded. The powder was then dried in a vacuum oven at RT for 24 h, followed by an additional drying step at 80°C for 24 h.

The structural and chemical characteristics of ZIF-8, MIL-140A, and MIL-101(Cr), including their formulas and pore dimensions, are summarized in Table S2 and in the Section S2 and Table S1.

2.1.5 | Characterization

Powder X-ray diffraction (PXRD) was performed using a Bruker D8 Advanced diffractometer with a Cu K_α source ($\lambda = 1.5418$ Å). The measurements were conducted over a 2θ range of 3–70, allowing for phase identification and crystallinity assessment. Thermogravimetric Analysis (TGA) was carried out using a Mettler Toledo 1600 TGA/SDTA851 under synthetic air conditions within a 30–800°C range, with a 100 mL/min gas flow rate. The pre-treatment involved heating at 30°C for 30 min, followed by a temperature ramp of 10°C/min up to 800°C, providing insight into the thermal stability of the materials. The morphological characterization of the MOF particles was conducted using Scanning Electron Microscopy (SEM) on a Jeol JSM-IT700HR. The imaging parameters used for SEM analysis are detailed in the corresponding figure. Energy Dispersive X-ray (EDX) analysis was performed using a Thermo Fisher Helios G4 UXe PFIB dual beam system. The EDX detector was an Ametek EDAX Octane Elite 65 mm, operated with the EDAX APEX EDS software suite, with acceleration voltages of 2 and 5 kV, and the beam current was 50 pA. Optical microscopy images of the chip and inks were captured using a Keyence VHX-600 digital microscope. MOF crystal structure images were generated by VESTA software, which is a three-dimensional visualization system for electronic and structural analysis.

Gas adsorption studies were carried out to evaluate the porosity and surface area of the MOFs. N_2 adsorption isotherms were obtained using a Micromeritics Tristar II at 77 K. Before the N_2 adsorption measurements, ZIF-8 was degassed under N_2 gas flow at 120°C for 16 h, while MIL-101(Cr) and MIL-140A were degassed under the same conditions but at 150°C for 16 h to ensure complete removal of adsorbed species. The BET surface area was calculated following Rouquerol criteria using the BETSI program [20, 21]. To study CO_2 uptake, CO_2 adsorption isotherms were recorded using a Micromeritics Tristar II at 298 K across a pressure range of 0-120 kPa. Before conducting CO_2 adsorption, ZIF-8 was degassed at 120°C for 3 h under N_2 flow, whereas MIL-101(Cr) and MIL-140A were degassed at 150°C for 3 h under N_2 gas flow. Water adsorption behavior was evaluated using a Micromeritics 3Flex Surface and Catalyst Characterization system at 293 K. Before the H_2O adsorption measurements, ZIF-8 was degassed in a vacuum degasser at 120°C for 16 h, whereas MIL-101(Cr) and MIL-140A were degassed in a vacuum degasser at 150°C for 16 h to eliminate any residual moisture. All adsorption isotherms have been converted to the AIF format and provided as Supporting Information [22].

2.2 | Functionalization by Inkjet Printing

2.2.1 | Ink Solvents

High-purity solvents were used in the ink formulation experiments. Ethanol (≥99.5%, Thermo Fisher) was used to prepare the inks, selected for its compatibility with the MOF materials and its effectiveness in dissolving the ink components. 2-propanol (≥ 99.7%, Sigma–Aldrich) was used for surface treatment of the CMOS chip.

2.2.2 | Ink Formulation

A commercially available Canon IJC257 UV-curable ink, referred to as UV ink, is used in this study. The ink is a mixture of multifunctional acrylate monomers/oligomers; mainly 3-methyl-1,5-pentanediol diacrylate, neopentyl-glycol diacrylate, 2-ethylhexyl acrylate, and trace acrylic acid, together with a benzophenone-type photoinitiator and proprietary additives. After UV exposure, the acrylate groups cross-link into a densely packed polyester/urethane network whose matrix is largely hydrophobic but still contains ester carbonyls that act as weak dipole sites. In this section, we explain how the MOF-based inks were prepared. To prepare the ZIF-8 ink, 0.5 g of dried ZIF-8 nanopowder was mixed with 2 mL of a 50:50 (v/v) water-ethanol solution. The mixture was sonicated for 20 min at an intensity of 270 W using a sonication probe in an ice bath to prevent overheating. The solution was then filtered using a 0.1 μm syringe filter to remove larger particles. A similar preparation method was applied for MIL-101(Cr) and MIL-140A. MIL-140A required a slightly longer sonication time of 60 min to achieve complete dispersion. Next,

2% (v/v) of the UV ink was added to the ink solution, followed by brief sonication to ensure thorough mixing using a Nanografi Ultrasonic Probe Sonicator at 30% power intensity in an ice bath to minimize mechanical and thermal damage to the MOFs. This step was observed to enhance the adhesion of MOF particles to the CMOS chip.

The final mixture consisted of 2% UV ink and 98% MOF suspension, a ratio selected to preserve accessibility to the MOF's high porosity, while ensuring compatibility with the inkjet printing process. This composition also helped maintain the MOF ink on the chip surface for an extended period and prevented MOF particles from detaching after drying. After printing on Si wafers or CMOS chips, an annealing process was performed using Memmert UN30 at 100°C for 30 min in air to eliminate residual solvents and improve film stability. The selection of low-boiling-point solvents, such as water and ethanol, in this study was intentional. This approach helps to avoid high-temperature annealing of the CMOS chip for extended durations, thereby preventing potential damage to wire bonding and electronic components. Moreover, higher annealing temperatures require a higher UV ink polymer content to ensure MOF stability on the CMOS chip. However, this increase in polymer content could negatively impact the porosity of the MOF-based ink and, consequently, its VOC selectivity.

2.2.3 | Substrate Pretreatment

Pristine (100) silicon or silicon/silicon dioxide (Si/SiO_2) wafers with a 300 nm thermal SiO_2 layer, a 4-inch diameter, a thickness of 525 ± 25 μm, and a resistivity of 10^3 to 10^5 Ω · cm were obtained from MicroChemicals (Germany). These wafers served for testing the inkjet printing parameters before starting the printing procedure on the CMOS chips. Before inkjet printing, the substrates were cleaned by sonicating them in acetone for 15 min, followed by 2-propanol (2IPA) for another 15 min. The substrates were then rinsed with deionized (DI) water and dried using an N_2 gun. It is important to note that no plasma treatment was applied to increase the surface hydrophilicity, in order to avoid potential electrostatic discharge (ESD) damage or degradation of the chip's wire bonds during vacuum plasma exposure.

Before inkjet printing on the CMOS chips, the chip surface was rinsed with 2-propanol and dried using a N_2 gun to remove any organic residues or dust, thereby ensuring optimal ink adhesion and print quality.

2.2.4 | Inkjet Printing Setup and Parameters

The PIXDRO LP-50 inkjet printer, equipped with Dimatix Materials Cartridge (DMC)-11610 cartridges, was used for the precise deposition of MOF nanoparticles and UV inks. This printer operates using a piezo-driven drop-on-demand mechanism, allowing fine control over the printing process with high resolution. The DMC printhead consists of 16 individually controlled nozzles, but in this study only a single 10 pL nozzle was activated for each ink.

The inkjet printing process was optimized for uniform deposition of UV and MOF-based inks on the CMOS chip and on Si/SiO_2 wafers. A piezo-actuated nozzle was used for each ink under different voltages and back-pressure conditions to ensure precise ink delivery. The distance between the print head and the substrate was set at 7.7 mm for the CMOS chip and 1 mm for the Si wafer, as these values provided optimal ink spreading and adhesion. The substrates were fixed on an x–y stage to prevent movement during printing, and all depositions were performed at room temperature (~29°C). After the printing process, UV curing was applied for 5 s using the built-in UV light source of the PIXDRO LP-50 to enhance ink adhesion and stability.

The detailed printing parameters are provided in Table 1, which lists the printhead type, voltage settings, print speed, ink pressure, resolution, droplet volume, and pulse-shape characteristics. The pulse-shape voltages and time durations (Idle Before, Fill Ramp, Time Low, Fire Ramp) are crucial factors affecting droplet formation and deposition quality. The UV ink and MOF-based inks (ZIF-8, MIL-101(Cr), and MIL-140A) were all printed using a DMC-11610 printhead, with the driving voltage, back pressure, and waveform timings optimized to generate stable, satellite-free droplets. This printing approach allows for the precise formation of ink patterns with minimal variation in thickness and ensures good repeatability across different printed attempts, as shown in Figure S13.

To further control ink deposition during printing, the printhead–substrate distance, print speed, and substrate temperature were kept constant for all prints, and droplet sizes and shapes were first optimized on Si/SiO_2 wafers before printing on the CMOS chip. Optical microscopy and FESEM images (Figure S10) and patterned arrays (Figure S13) confirm well-defined circular droplets and uniform droplet distributions, ensuring a reproducible deposited volume per droplet. On the CMOS chip, the number and spacing of droplets per functional region are defined in the printing software so that each region receives a controlled number of overlapping droplets, leading to a consistent effective coating thickness over the selected pixel ensembles (see also Figure 5b–g; Figure S15).

Although single-droplet FESEM images on SiO_2/Si (Figure S10f) show a ring-like profile indicative of a coffee-ring effect, the actual coatings on the CMOS chip are formed by overlapping many droplets to create continuous films over ensembles of pixels. The resulting lateral response maps in Figure 5b–e and the averaging over selected regions (Figure 5f–g) demonstrate that, at the scale of the sensing pixels, the coatings are effectively homogeneous and do not exhibit detectable electrical response segregation. Remaining non-uniformities can be corrected for by calibration measurements at the individual pixel level.

2.3 | VOCs Gas Sensing Setup of Pure and Mixed VOCs

In this study, the pixelated capacitive sensor (PCS) CMOS platform detects VOCs via adsorption-induced permittivity changes in inkjet-printed MOF/polymer layers on capacitive pixels. This capacitive transduction is fundamentally different from the O_2-driven band-bending mechanism of resistive metal-oxide sensors [23]. Consequently, under dry conditions, dry synthetic air (O_2 in

TABLE 1 | Printing recipes for the inks.

Parameter	UV Ink	ZIF-8 Ink	MIL-101(Cr) Ink	MIL-140A Ink
Printhead	DMC 11610	DMC 11610	DMC 11610	DMC 11610
Voltage Raw B	40	40	40	100
Print speed (mm/s)	50.8	50.8	50.8	50.8
Ink pressure (mbar)	−1	−6	−5	−5
Resolution (DPI)	500	500	500	500
Native droplet volume (pL)	10	10	10	10
Measured droplet volume (pL)	9	8.9	9.2	9.3
Nozzles used during printing	1	1	1	1
Pulse Shape Voltages (V)				
High Voltage	27	25	20.0	26
Medium Voltage	9	13	13.0	9
Low Voltage	3	3	1.5	3
Pulse Shape Time Duration (μs)				
Up Down	0.1	0.1	20.0	20.0
Idle Before	6	0.5	3.0	0.5
Fill Ramp	5	0.5	3.0	3.0
Time Low	6	1	6.0	10.0
Fire Ramp	2	4	2.4	2.4
Time High	3	0.5	2.0	2.0
End Ramp	5	0.5	2.0	2.0
Idle After	7	10	5.0	5.0

N_2) and dry N_2 are expected to yield equivalent PCS responses. We verified this at the outset (dry synthetic air vs. dry N_2) and observed indistinguishable signals; therefore, all subsequent measurements used dry N_2 as the carrier at constant total flow.

The CMOS sensor chip operated at a self-heated steady temperature of 30 ± 1 °C, measured on the package adjacent to the die (thermocouple). The chamber air was 23 ± 2 °C.

The VOC gas sensing experiments were conducted using a controlled exposure system, as illustrated in Figure 1. The system comprises a VOC bubbler, a dilution stage, and a test chamber where the sensor is positioned for real-time measurements. This setup is designed to test both pure and mixed VOCs under controlled environmental conditions. The switching time remains fixed throughout the experiment to systematically evaluate the ON/OFF behavior of the sensor. Figure S14 shows a photograph of the actual experimental gas sensing setup.

The setup operates by pumping N_2 through three individual pumps, numbered I-III, using independent syringe pumps (NE-4000 Two Channel). The setup operates by delivering dry N_2 via three independently controlled syringe pumps (NE-4000 Two Channel), designated I–III. The carrier gas is dry N_2 at a constant total flow (maintained throughout the experiments).

Pump II is designated for VOC_1 (for pure gas measurements), while pump III is reserved for VOC_2 (in cases of mixture experiments). The entire setup utilized standard microfluidic polytetrafluoroethylene (PTFE) tubing (1/16" OD × 1/32" ID). Pump I is used for dilution in both pure and mixing experiments. The flow rate over the CMOS capacitive sensor array chip is kept constant at 2 mL/min throughout the entire experiment. Note that pumps II and III each contain two identical syringes filled with N_2. Consequently, pump II and pump III deliver equal volumetric flow rates, $\dot{V}_2$ and $\dot{V}_3$, respectively, which are split into two branches: one branch passes through the VOC bubbler, while the other bypasses the bubbler(s).

To efficiently generate vapor at the saturated pressure (P_s), we used a two-stage bubbling train (glass bottles) followed by a third, empty knock-out bottle to prevent VOC condensate from reaching the sensor chip. The physical and chemical properties of all VOCs in this study, including their P_s, are summarized in Table 2. Where all solvents were of high purity: Ethanol (≥99.5%, Thermo Fisher) and 2-Propanol (≥ 99.7%, Sigma–Aldrich), Methanol (≥99.9%, Honeywell), 1-Butanol (≥ 99.4%, Sigma–Aldrich), 2-butanone (≥99.5%, Sigma–Aldrich), and toluene (≥ 99.8%, Merck) were used in the gas-sensing studies.

The experiments were conducted at a constant temperature of 1°C, maintained using an ice bath, and precisely controlled via a thermocouple. By controlling the temperature, we can estimate the saturated vapor pressure of the gas using the Antoine equation (see Section S1), and use this to estimate the VOC

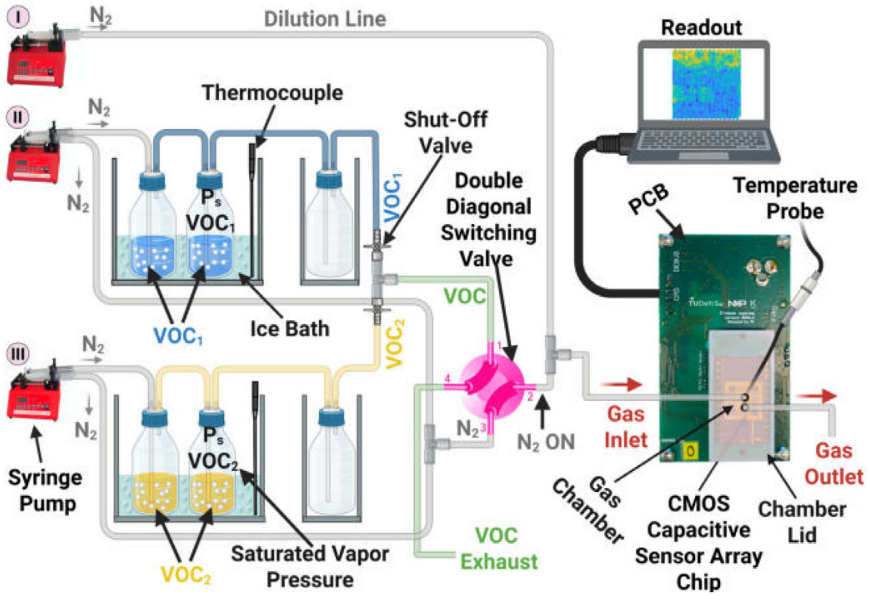

FIGURE 1 | Pure and mixed VOCs gas sensing setup. The setup comprises three syringe pumps (I–III) that deliver N_2 to the dilution, VOC_1, and VOC_2 channels, respectively. Each VOC channel includes a shut-off valve to select VOC_1, VOC_2, or their mixture. A four-way diagonal valve (shown in pink) switches the flow sent to the sensor between pure N_2 and N_2 mixed with VOCs. The schematic depicts the pure N_2 case. To expose the chip to a VOC_1/VOC_2 mixture, rotate the diagonal valve by 90° to enable VOC delivery. The experimental setup is shown in Figure S14.

TABLE 2 | Physical and Chemical Properties of VOCs. MW: Molecular weight (g/mol), Ps: Vapor pressure at 1°C (mmHg), DC: Dielectric constant, MD: Molecular diameter (Å), BP: Boiling point (°C), DM: Dipole moment (D), P: Polarity, SI: Solubility interactions.

VOC	MW	Ps [24]	DC [25]	MD	BP	DM	P	SI [26]
Ethanol	46.07	15.23	24.55	~4.4	78.0	1.69	Polar	**Dipolarity, Hydrogen Bonding**
2-IPA	60.10	8.96	18.3	~4.8	82.0	1.66	Polar	**Dipolarity, Hydrogen Bonding**
Methanol	32.04	31.51	32.7	~4.0	65.0	1.70	Polar	**Acidity, Dipolarity**
Water	18.02	4.89	78.3	~3.1	100.0	1.85	Highly Polar	**Strong Hydrogen Bonding, Acidity**
2-butanone	72.11	26.70	18.5	~4.5	79.6	2.78	Polar	**Dipolarity, Weak Hydrogen Bonding**
1-Butanol	74.12	1.72	17.8	~5.1	117.7	1.66	Polar	**Dipolarity, Hydrogen Bonding**
toluene	92.14	7.54	2.38	~5.8	110.6	0.37	Non-Polar	**Polarizability, Dispersion Forces**

concentration in the gas flow. A third bottle after the 2 bubbler is used to bring the gas to room temperature. Before each experimental run, pure dried nitrogen was flushed through the system for one hour to remove any residual gases and prevent humidity accumulation. Simultaneously, the bubblers were activated to ensure the VOCs reached their saturated vapor pressure before entering the measurement setup. We change the volume flow rates of the pumps to reach the desired concentrations as explained in equations Equation (2) and Equations (S1).

During the measurement process, a four-way diagonal valve (IDEX 4-Port Switching Valve) was used to switch between exposing the sensor to VOC vapors and pure N_2. The valve and pump settings are configured such that we ensure the gas flow rate over the sensor is constant during the experiment, with only the composition of the gas being changed. This reduces flow-rate-dependent effects on the sensor response. Multiple microfluidic Y connectors made of PEEK were used to connect the different lines.

During the gas sensing experiments, the gas concentrations and of both VOC1 and VOC2 are varied by controlling the flow rates $\dot{V}_2$ and $\dot{V}_3$ using syringe pumps II and III, while the flow rate $\dot{V}_1$ of pump I is adjusted to maintain the total gas rate over the sensor constant at $\dot{V}_{\text{total}} = 4$ mL/min according to this equation:

$$\dot{V}_{\text{total}} = \dot{V}_1 + \dot{V}_2 + \dot{V}_3 = 4\ \text{mL/min}. \quad (1)$$

To calculate the concentration of each of the VOCs on the sensor surface, we first need to calculate its concentration after it leaves the bubbler. For this purpose, we use the Antoine equation to determine the saturated vapor pressure P_s of the VOC at the temperature of the ice, and then use the following equation to determine the VOC concentration that reaches the sensor:

$$C_{\text{VOC1}} = \frac{P_{s,1}}{P} \times \frac{\dot{V}_2}{\dot{V}_{\text{total}}} \times 10^6\ \text{ppm} \quad (2)$$

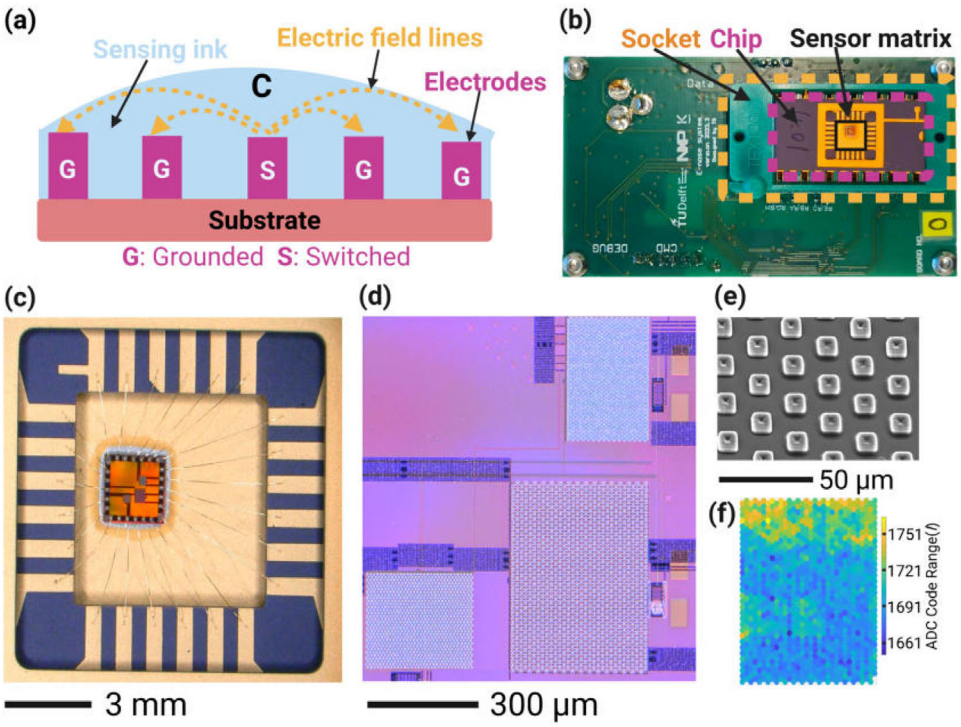

FIGURE 2 | Working principle and CMOS pixelated sensing chip. (a) Working principle of the capacitive gas sensor. The capacitance changes when exposed to VOCs due to the effect of the gas on the dielectric constant of the sensing ink. A more detailed CMOS device cross-section is shown in Figure 3. (b) Packaged CMOS pixelated sensing chip mounted on readout PCB (c) Close-up optical image of the CMOS pixelated chip in a ceramic package. (d) Microelectrode arrays of the pixelated capacitive sensing chip. The dimensions of the microelectrodes in the three sensor matrices are shown in Figure S15. (e) SEM top-view image showing the pixelated microelectrode structures. (f) Display of the capacitance distribution over all 1024 pixels, with corresponding ADC values indicated by the colorscale.

Where C_{VOC1} is the VOC concentration, $P_{s,1}$ is the saturated vapor pressure of VOC1 at 1 °C as determined from the Antoine equation (see Section S1), and P is the atmospheric pressure. The first factor in Equation (2) accounts for the concentration of the VOC in the bubbler, while the second factor accounts for the dilution by mixing with the nitrogen flow. For VOC2 the equation becomes $C_{VOC2} = \frac{P_{s,2}}{P} \times \frac{\dot{V}_3}{\dot{V}_{total}} \times 10^6$ ppm.

3 | Results

3.1 | Working Principle and E-nose Chip Electronics

The capacitive E-nose operates by detecting capacitance variations between its electrodes that are caused by changes in the dielectric properties of the sensing ink upon exposure to VOCs. The working principle and CMOS pixelated chip design are illustrated in Figure 2, showcasing both the functional mechanism and the hardware integration.

The operation mechanism is illustrated in Figure 2a. Under reference conditions, where only N_2 gas surrounds the sensor, the sensor detects a reference capacitance value (C_0). However, when exposed to VOCs, interactions of the gas with the sensing ink lead to a change in the effective dielectric constant [12], thereby changing the capacitance to ($C_0 + \Delta C$). Microscopically, this capacitance change can originate from changes in the charge, conductivity, and dielectric constant distributions in the ink that change its effective dielectric constant when the gas molecules diffuse through the material or adsorb on the porous surface of the functional layer. By engineering functional layers whose effective capacitance is affected more by certain gases than by others, the sensor's selectivity can be enhanced. The capacitance changes are detected by switching the voltage on the switch (S) electrode between 0 and 0.9 V at a frequency of 40 MHz. This causes a capacitive current proportional to the capacitance between the S and G (grounded) electrodes (See Figure 1a), which is digitized by an analog-to-digital converter (ADC) in the CMOS chip.

In this work, we describe the CMOS pixelated sensing chip and readout electronics that we designed, fabricated used for gas sensing, utilizing the described capacitive operation principle. Photographs and micrographs of the capacitive pixelated CMOS E-nose are shown at different magnifications in Figure 2b–e and in Figure 3. Figure 2b presents the printed circuit board (PCB), with a socket for mounting the packaged CMOS pixelated sensing chip, providing a USB connection between the sensor array and a computer. Figure 2c shows an optical image of the CMOS chip that is mounted in a ceramic package and electrically connected by bondwires.

The pixelated capacitive sensor array that resembles our work most is the recently reported MOF-integrated e-nose that realizes high-density pixel arrays with a pixel dimension of 45×45 µm^2

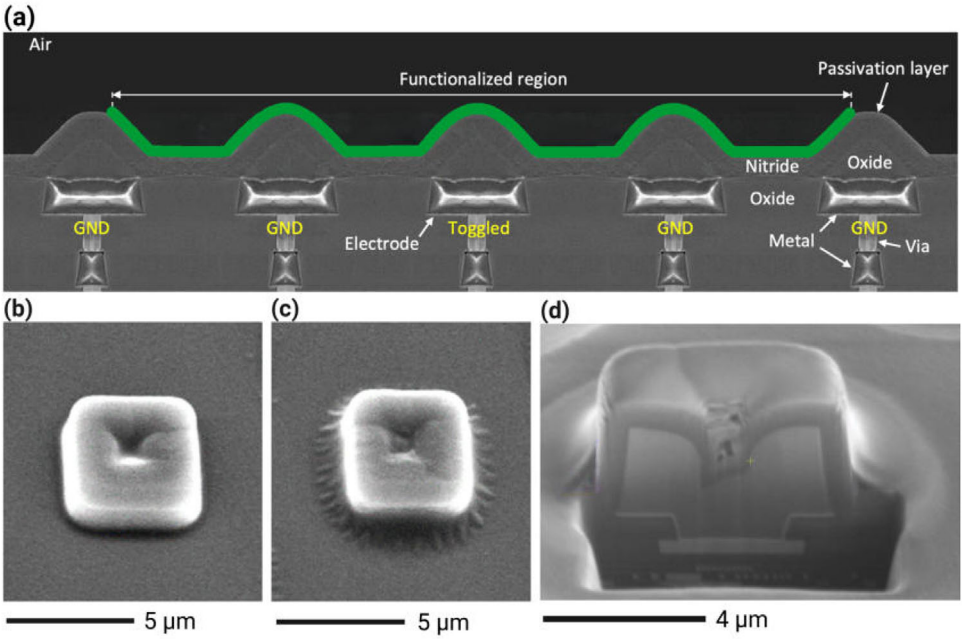

FIGURE 3 | Artist impression, based on SEM images, of cross-section of CMOS sense electrodes by sensing ink. (a) The electrodes, made in the top-metal layer of the CMOS process, are connected vertically by vias and intermediate metal layers to pairs of switching transistors at the bottom (not visible). The middle electrode is selected by toggling (switching) its potential between 0 and 0.9 V at high frequency. This makes it the active plate of the selected sense capacitor. Electric field lines emerging from it pass through the green sensing ink and terminate mainly on grounded adjacent electrodes that collectively constitute the counter electrode plate of the selected sense capacitor. Note that Figure (a) is an artist's impression that has been constructed by cut-and-pasting SEM cross-section images from various parts of the chip. (b) SEM image of a reference bare electrode. (c) SEM image of a functionalized electrode with a UV ink. Note that one ink droplet covers several electrodes. (d) A focused-ion-beam (FIB) SEM cross-section image of a single electrode pixel. Thinner CMOS backend metal layers that connect the pixel to the transistors are visible below the thick top electrode. An ink meniscus is adhering to the edges on both sides of the pixel.

(electrode spacing ~2 µm), operating at 156.25 kHz [27]. The platform features 4096 pixels with integrated temperature sensors and heaters for recovery. In this work we present a platform that features 3 pixelated matrices, each having 1024 capacitive pixels, operating at 40 MHz, enabling detecting capacitance changes less than 1 aF. The smallest pixel dimensions are 4×4 μm^2 with a pixel spacing of 10µm. Furthermore, all sensing layers are deposited by solution-based inkjet printing directly onto the passivated CMOS surface, providing a wet-process-compatible and purely additive route to multi-material functionalization. The same printing workflow can be extended to larger arrays and a broader range of inks without additional lithography or etching steps, which is advantageous for low-cost, scalable deployment of high-diversity e-nose systems.

Figure 2d highlights the three pixelated microelectrode sensing matrices on the chip, which serve as the detection interface where the sensing functional layer interacts with VOCs. This figure shows three distinct sensor matrices, each designed with different electrode geometries to support various sensing configurations. Sensor Matrix 1 (bottom right) consists of square electrodes with dimensions of 5×5 μm and an interelectrode spacing of 15 μm. Sensor Matrix 2 (top right) features electrodes with dimensions of 4×4 μm and an interelectrode spacing of 10 μm, while Sensor Matrix 3 (bottom left) has electrodes of 5×5 μm with an interelectrode spacing of 10 μm. These different sensor matrices were designed to investigate and optimize the electrode design. The experiments in this work were performed using Sensor Matrix 1. Details on the electronic design and CMOS fabrication process can be found in refs. [17, 28].

Figure 2e displays a top-view SEM image of the microelectrodes in Sensor Matrix 1, and Figure 3 an image of their cross-section, illustrating the structural topography of the sensing electrodes. The undulating surface of the CMOS chip, characterized by valleys around the electrodes, is a direct result of the CMOS fabrication process, where silicon-oxide and silicon-nitride passivation layers protrude upward at the location of the electrodes. The capillary forces in the valleys between these protrusions help localize the printed ink in the areas between the microelectrodes, as will be explained in the next section.

Figure 2f demonstrates the pixelated sensor readout, showing a spatial map of the measured response by each of the pixelated electrodes under exposure to VOC. The color scale-bar indicates the ADC capacitance readout value under VOC exposure. The ink-coated areas exhibit a stronger capacitance change (yellow pixels) compared to the non-coated areas (dark blue pixels).

To electronically read-out the pixelated sensor, the E-nose chip contains analog-to-digital converters (ADC) that convert the capacitive signals to digital ADC values that are sent by the chip via the PCB and USB connection to the computer. For this purpose, the capacitive current is amplified by a factor of 100 by a current mirror, after which the voltage it generates across a 68 kΩ

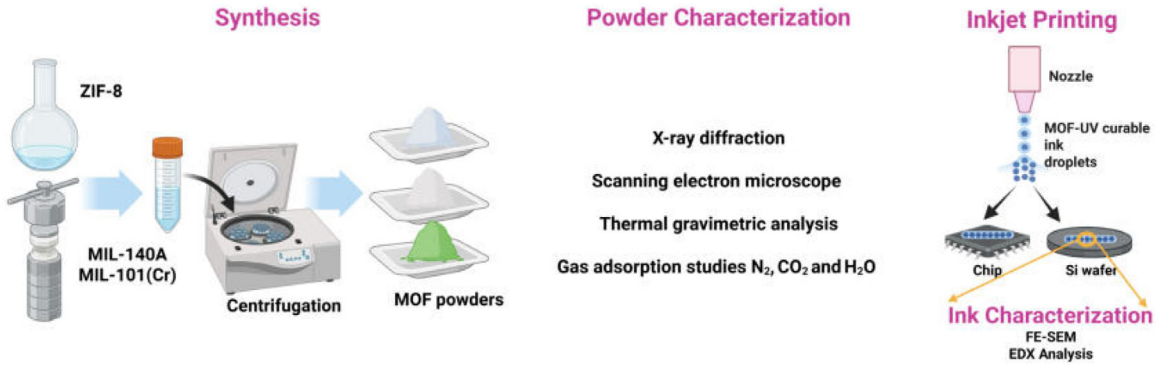

FIGURE 4 | Graphical summary of the material synthesis, deposition, and characterization. Various MOF powders, which are selected for their gas sensing potential, were synthesized, characterized, and mixed with ethanol/water solvent to make them printable ink. Later, it was mixed with UV-light curable ink to improve the stiction of the MOFs to the sensor array. Droplets of the mixed inks containing the MOF powder are inkjet printed on the sensor chip, UV cured, and characterized. The details of these steps, and the improvement of the ink formulation, can be found in Section 2.

resistor is digitized by a 12-bit (4096 values) ADC. With respect to a calibrated reference ADC value ADC_{ref}, the relationship between the digital ADC readout and the measured capacitance $C_{measured}$ of the sensor is given by:

$$C_{measured} = \frac{1}{100 \times 0.9\,V \times 40\,MHz \times 68\,k\Omega} \times \left[\frac{(ADC_{output} - ADC_{ref}) \times 3.3\,V}{4096}\right] \quad (3)$$

According to this equation, a change of 1 in the value of ADC_{output} corresponds to a capacitance change of 3.3 aF of the sensor, and the 12-bit capacitance detection range is 4096×3.3 aF = 13.5 fF. Note that by averaging, even smaller capacitance changes can be achieved, as shown in Section S4.2. A dedicated MATLAB code has been developed to analyze pixelated responses, as shown in Figure S16, and to generate figures such as Figure 2f. The software enables continuous analysis of the average capacitance change over user-selected sets of pixels, e.g., to separately analyze and compare the effect of gases on functionalized and non-functionalized electrode areas in different parts of the pixelated array.

The effective thermal noise is reduced by averaging the responses of multiple pixels covered by the same functional layer and by applying a moving average over time to the resulting traces. No further digital filtering is used, thereby preserving all relevant dynamic features of the sensor response. From repeated measurements in nitrogen, the standard deviation of the residual noise in Figure 7 corresponds to an input-referred capacitance fluctuation of approximately 1 aF per sensor element, which is already very small compared to the baseline capacitance.

3.2 | Sensor Functionalization by Inkjet Printing

The pixelated capacitive sensor array is functionalized via direct inkjet printing of pre-synthesized MOF [29]. The functionalization workflow is summarized in Figure 4. It illustrates Metal–Organic Framework (MOF) synthesis, characterization, ink formulation, inkjet printing, and printed ink analysis. The details of the material preparation and characterization are described in Section 2 and Sections S2, and S3. The synthesized MOFs, namely ZIF-8 (*zeolitic imidazolate framework-8*), MIL-101(Cr) (*Materials of Institut Lavoisier-101, chromium; Cr(III) terephthalate*), and MIL-140A (*Materials of Institut Lavoisier-140A; Zr(IV) terephthalate*) were structurally analyzed using X-ray diffraction (XRD), scanning electron microscopy (SEM), and Thermogravimetric analysis (TGA) before being formulated into Ultraviolet (UV)-curable inks for printing onto Silicon wafer and chip. The printed structures were characterized by field emission scanning electron microscopy (FE-SEM) and energy-dispersive X-ray (EDX) analysis. To evaluate sensor selectivity, we tested a panel of VOCs and additionally measured hydrophobicity as explained in the next sections.

The structural and adsorption analyzes of the MOFs ZIF-8, MIL-101(Cr), and MIL-140A are discussed in detail in Section S2. Further discussion focusing on ZIF-8 and the UV-curable inks is provided in more detail here. To functionalize the chip, ZIF-8 ink was pre-mixed with UV ink at a 2:98% mixing ratio. Initially, inkjet printing parameters were optimized for droplet shape, distribution, and diameter by printing on SiO_2/Si wafers. The optical microscopy images of both inks are shown in Figure S10, revealing well-patterned circular droplets with average diameters of $29.9 \pm 0.2\,\mu m$ for the UV ink and $64.7 \pm 0.9\,\mu m$ for the ZIF-8 ink

To further assess printing uniformity, additional patterned arrays were inkjet-printed on SiO_2/Si wafers for both inks, as shown in Figure S3.3. These patterned matrices demonstrate a uniform droplet distribution, highlighting the inkjet printing process's repeatability, uniformity, and precision. Surface characterization of the individual droplets containing ZIF-8 nanoparticles was carried out using FE-SEM, as shown in Figure S11. The FE-SEM images confirm that the ZIF-8 nanoparticles retain their expected morphology, consistent with their structure before printing, as depicted in Figure S12. EDX analysis was conducted on the total EDX intensity images of the inkjet-printed UV and ZIF-8 inks. Elemental mapping results of a selected area for UV and ZIF-8 inks are shown in Figure S12c,d, confirming the successful printing and uniform elemental distribution within the deposited inks.

EDX analysis was conducted to investigate the total EDX intensity image of the inkjet-printed UV and ZIF-8 inks. Selected area analysis and the corresponding spectrum for the UV ink (Figure S12a,c) confirm the presence of carbon (C), nitrogen (N), and oxygen (O), as expected for the organic matrix. For ZIF-8, the grayscale elemental mapping in Figure S12b,d highlights the distribution of zinc (Zn), O, and C across the printed area at high magnification. Zn appears to be well-distributed throughout the scanned region.

After optimizing the printing conditions on Si wafers, the inkjet printing process was applied to CMOS microelectrode chips. Figure 5a shows 4 droplets of UV ink and 4 droplets of ZIF-8 ink deposited on Sensor Matrix 1 by inkjet printing; the droplets are observed to cover roughly circular regions on the chip having a diameter of around 50 μm. The layer thickness and surface coverage are not always optimal, as is e.g. visible in the UV ink droplet on the bottom-right of Figure 5a. Therefore, to increase ink layer height and chip coverage uniformity, we deposit multiple ink droplets at the same position to improve sensing signals.

3.3 | Measurement Method

To illustrate the basic operation principle of the pixelated capacitive sensor (PCS) array, Figure 5b–e, illustrate the spatial distribution of the capacitance change ΔC under various gas exposure conditions. The colorscale indicates $\Delta\mathrm{ADC}_{\mathrm{output}} = \mathrm{ADC}_{\mathrm{output}}(t) - \mathrm{ADC}_{\mathrm{output}}(t_0)$, the difference between $\mathrm{ADC}_{\mathrm{output}}(t)$ and the reference at t_0, the difference of the value of $\mathrm{ADC}_{\mathrm{output}}(t)$ compared to its reference value in nitrogen gas at atmospheric pressure at the start of the measurement sequence at time t_0. Figure 5b shows the sensor response in a nitrogen environment, with the observed spatial variations giving a qualitative impression of the sensor stability. Figure 5c,d highlight the localized sensor responses of UV ink and ZIF-8 ink when exposed to toluene (methyl benzene, $C_6H_5CH_3$) and 2-butanone (methyl ethyl ketone, $CH_3C(O)CH_2CH_3$), respectively. The UV ink shows the strongest response to toluene, while the ZIF8 ink shows the strongest response to 2-butanone. When both VOCs are present together, as shown in Figure 5e, both inks exhibit a response, confirming the sensor's ability to detect VOCs individually and in a mixture. This demonstrates that our pixelated CMOS microarray is a multi-sensing platform for detecting multiple VOCs by integrating different ink materials. Each ink selectively interacts with specific VOCs, enabling continuous detection of multiple gases with the same sensor matrix.

In the final transducer configuration shown in Figure 5b–g, only two functional layers are therefore used on the CMOS array: a ZIF-8 ink region and a region coated with the neat UV-curable resin, which serves as the polymer reference. MIL-101(Cr) and MIL-140A were employed in the initial humidity-screening experiments (Figure 6a,b) but were not used in the final VOC calibration and mixture measurements because their strong water uptake leads to large humidity cross-sensitivity outside the scope of the present study.

To evaluate the response of only specific pixels that are located beneath the ink's functionalized layer, software allows users to manually select the relevant pixels and is programmed to average the value of $\Delta\mathrm{ADC}_{\mathrm{output,f0}}$ of the selected pixels Figure 5f,g, which is then plotted in the graph of the sensor response. The same software is also used to select and average the ADC value over an empty, non-functionalized region on the chip to get $\Delta\mathrm{ADC}_{\mathrm{output,empty}}$. Then the average and background subtracted response of the functionalized region is calculated using $\Delta\mathrm{ADC}_{\mathrm{output,f}} = \Delta\mathrm{ADC}_{\mathrm{output,f0}} - \Delta\mathrm{ADC}_{\mathrm{output,empty}}$. This averaging procedure over a large number of the (in total) 1024 sensing pixels significantly reduces noise.

3.4 | Demonstration of Gas Sensing in Pure Gases and Gas Mixtures

A dedicated setup was used to control individual gas concentrations of the two VOCs in a nitrogen gas background flow. Details of this setup and the experimental procedure can be found in the experimental section (Figure 1) and Section 2.3.

This setup measures the humidity responses of various MOFs and evaluates VOC selectivity; details are provided in the following sections.

3.4.1 | Humidity Response

For many applications, such as greenhouses and animal farms, it is important that the E-nose signal is independent of the air humidity level. For this purpose, it is important to verify the response of the sensor to humidity for different functionalization inks. It is expected that hydrophobic sensing materials can reduce the effect of humidity variations on the E-nose reading.

To check the response to humidity, the sensor was exposed to nitrogen gas that was humidified with 6000 ppm of water vapor. The test was performed for MIL-101(Cr), MIL-140A, ZIF-8, and UV inks. The real-time response curve in Figure 6a shows the ADC readout of MIL-101(Cr), MIL-140A, ZIF-8, and UV ink. Upon water vapor exposure, MIL-101(Cr) and MIL-140A exhibit a significant increase in response, indicative of a high water adsorption capacity.

In contrast, ZIF-8 and the UV ink exhibit only minor capacitance shifts, confirming a more hydrophobic nature and lower humidity cross-sensitivity. This trend matches the water-sorption isotherms of the MOFs: ZIF-8 takes up virtually no H_2O until ~80% RH, ZIF-8 takes up virtually no H_2O until ~ 80% RH (Figure S2c), in agreement with previous computational and adsorption studies [30–33]. Whereas MIL-140A and MIL-101(Cr) adsorb progressively across the RH range (Figures S5c and S8c).

In these tests, the water concentration of 6000 ppm corresponds to ~ 20% relative humidity at 23 °C, i.e., a typical lower end of indoor humidity. The small capacitance changes observed for ZIF-8 and the UV ink at this level are consistent with the independent powder water adsorption isotherms: ZIF-8 remains essentially dry up to ~ 80% RH (Figure S2c), whereas MIL-101(Cr) and MIL-140A show much higher water uptake (Figures S8c and S5c) and were therefore not used in the final VOC calibration and mixture experiments.

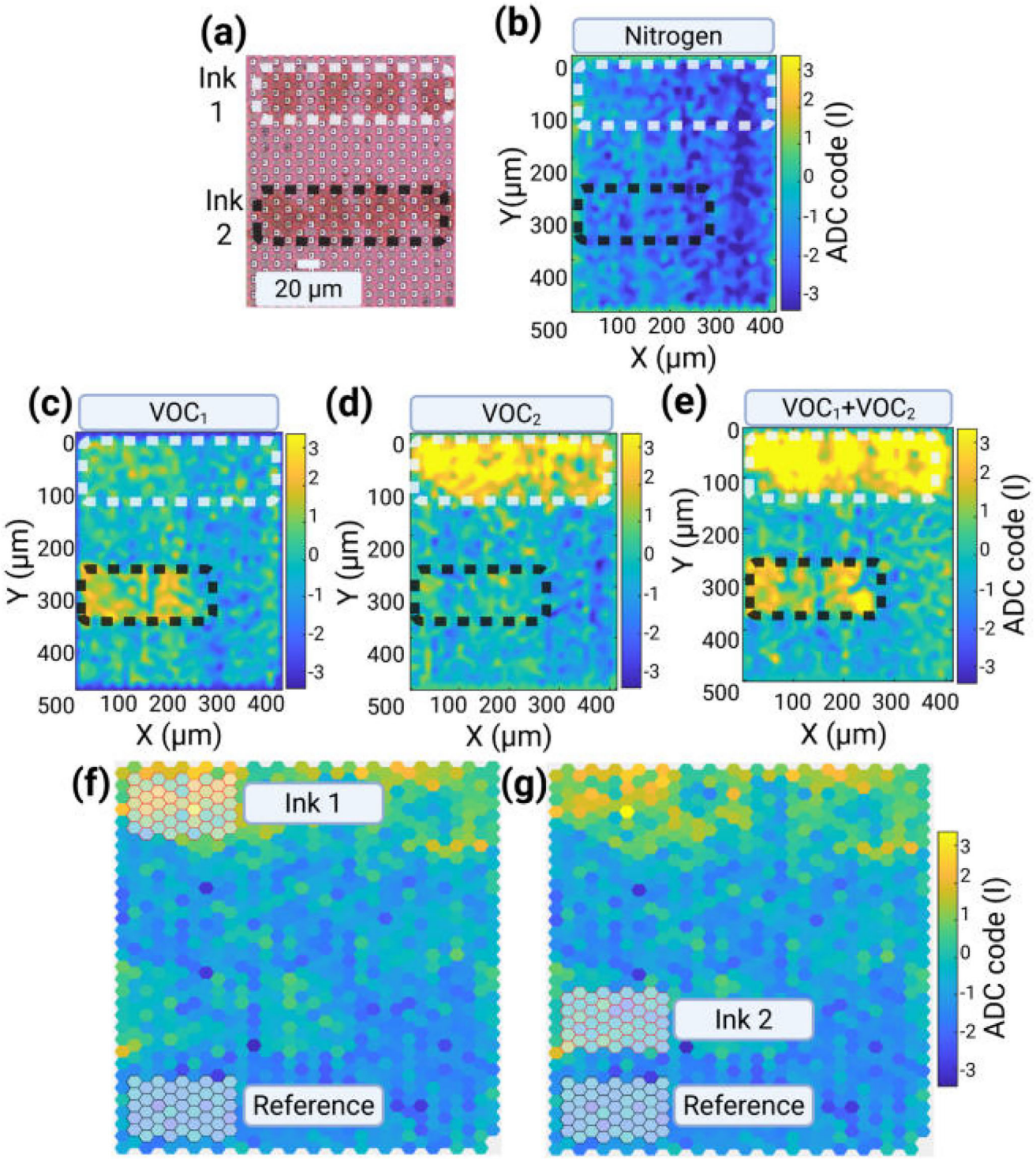

FIGURE 5 | Sensor response of the pixelated sensor matrix to VOCs after functionalization by inkjet printing. (a) Optical microscopy image of inkjet-printed ZIF-8 (ink 1) and UV-curable ink (ink 2) single droplets spaced by 15 µm on part of the CMOS microelectrode array. Details of the microelectrode-array structures for the different sensor matrices are explained in Figure S15. The image shows individual droplets after UV light curing, followed by multiple droplet depositions, leading to their merging as in (b-e). (b–e) Lateral distribution of the capacitance change ΔADC_{output} under gas conditions. The scale bar represents the change in the ADC code (I), where 1 ADC code represents a capacitance change of 3.3 aF as expressed in Equation (1). The dashed lines indicate different ink regions: ZIF-8 ink (white) and UV ink (black). This sensor chip is different from that shown in (a). (b) Response under N_2 (reference). (c) Exposure to toluene. (d) Exposure to 2-butanone. (e) Mixed toluene and 2-butanone exposure. (f,g) Selected regions over which ADC values are averaged for determining $\Delta ADC_{output,t_0}$ for ink 1 and ink 2 functionalized areas and $\Delta ADC_{output,empty}$ in the reference region.

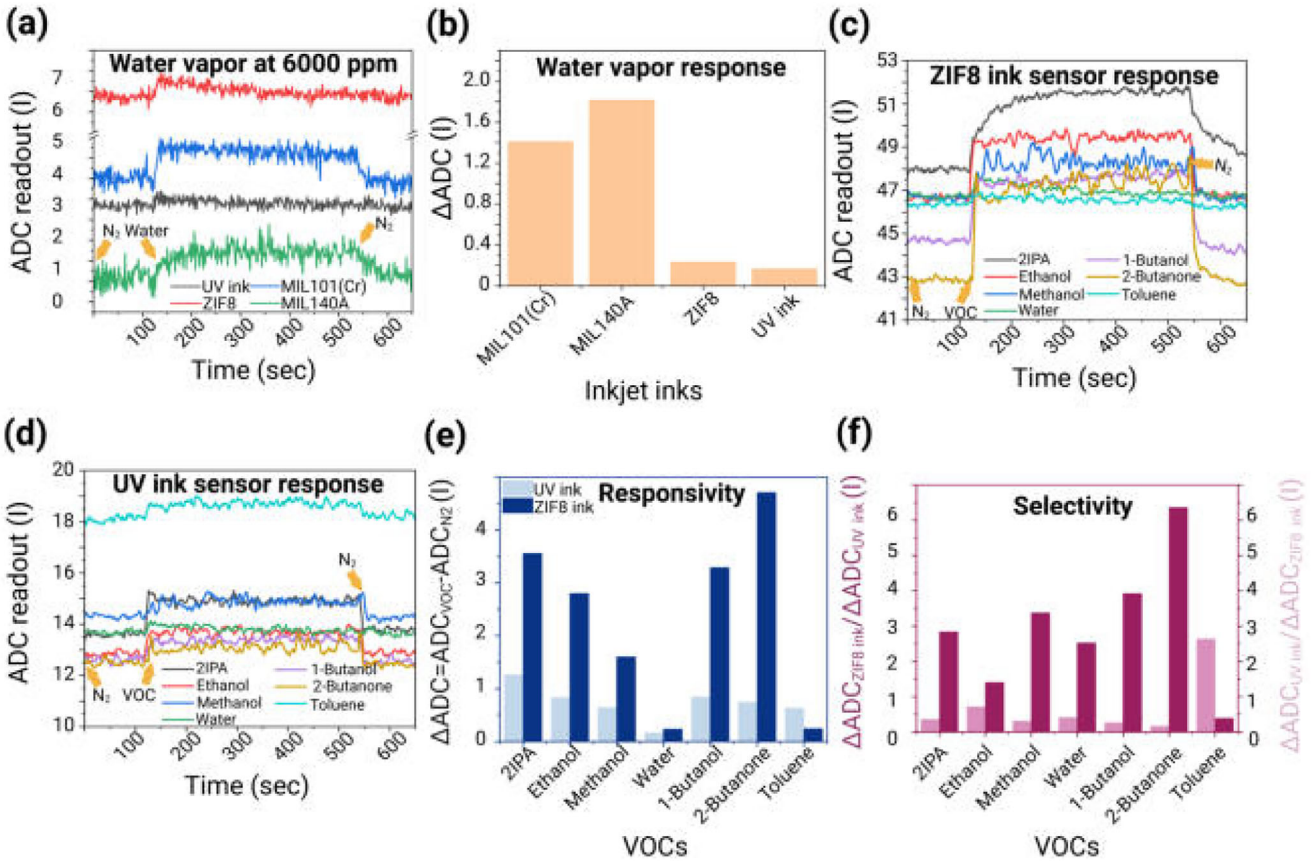

FIGURE 6 | Water vapor and VOC selectivity analysis of different MOFs. (a) Dynamic ADC response of MIL-101(Cr), MIL-140A, ZIF-8, and UV ink under exposure to 6000 ppm water vapor. Arrow lines indicate the switching between the N_2 baseline and water vapor exposure. To reduce electronic noise, signals are averaged over a large number of pixels, which affects noise but not the actual sensor response. (b) Quantified water vapor response of inkjet printed samples calculated as the difference in ADC signal between steady-state exposure to water vapor and the baseline under dry N_2. Higher values indicate higher water adsorption, reflecting the relative hydrophilicity of the sensing materials. (c) Dynamic sensor responses of UV ink toward different VOCs. (d) Dynamic sensor responses of ZIF-8 ink toward different VOCs. (e) sensor response of UV ink and ZIF-8 ink upon VOC exposure. Bars show $\Delta ADC = ADC_{VOC} - ADC_{N_2}$ (I); light blue corresponds to the UV ink and dark blue to the ZIF-8 ink. Higher ΔADC values indicate stronger responsivity toward the analyte. (f) Selectivity of the two inks toward individual VOCs, defined as the ratio of their responses. Dark bars (left axis) plot the ratio $\Delta ADC_{ZIF\text{-}8\ ink}/\Delta ADC_{UV\ ink}$ and identify analytes for which the ZIF-8 ink is more responsive. Light bars (right axis) show the reciprocal ratio $\Delta ADC_{UV\ ink}/\Delta ADC_{ZIF\text{-}8\ ink}$ and identify analytes for which the UV ink is more responsive.

The low water response of the UV ink can be rationalized by its composition and cross-linked structure. The cured film is a dense polyester/urethane network formed from multifunctional acrylate monomers and oligomers (Section 2.2.2), with a very high aliphatic carbon content (97.5 wt.% C and only 1.6 wt.% O, see Table S3 and Figure S12). This implies a predominantly non-polar environment with only a sparse distribution of polar ester carbonyl groups and hydrogen-bonding sites. The resulting hydrophobic matrix suppresses strong water sorption but still allows appreciable uptake of apolar VOCs such as toluene, as evidenced by the stronger capacitance response of the UV-ink layer to toluene compared to 2-butanone in Figure 7g.

Figure 6a displays the full time-resolved response, while Figure 6b shows a histogram of the averaged ΔADC between 6000 ppm water vapor and the dry N_2 baseline.

These observations can be accounted for by the large hydrophilic cages of MIL-101(Cr) and the 1-D channels of MIL-140A that host open metal sites and hydroxylated surfaces, promoting strong water uptake. MIL-101(Cr) offers Cr^{3+} coordinatively unsaturated sites, whereas MIL-140A presents Zr–OH groups; both act as potent hydrogen-bond donors/acceptors (see Section S4 for details).

These results confirm that ZIF-8 and UV ink are advantageous for gas sensing in humid environments because of their lower response to water vapor. Given their reduced water-vapor response, ZIF-8 and the UV ink were chosen for the subsequent gas-sensing measurements.

3.4.2 | VOC Response

E-nose responses to several VOCs were measured to assess the selectivity of the ZIF-8 and UV-based functional layers. In addition to the MOF-based inks, the neat UV-curable resin (without MOF nanoparticles) was also printed on the CMOS chip and used as a polymer layer. This UV ink was subjected to the same humidity and VOC exposure protocols as the ZIF-8

ink, enabling direct comparison of the polymer matrix response with that of the MOF-loaded composite. No additional polymer matrices were investigated in this study. Figure 6c–f presents the dynamic responses of ZIF-8 ink toward different VOCs, including 2-propanol (2IPA), ethanol, methanol, water, 1-butanol, 2-butanone, and toluene. The ADC readout is plotted against time, illustrating the sensor's behavior during exposure to each VOC and subsequent N_2 purging. Water exhibits the weakest response, confirming that only a trace amount is adsorbed in the framework. The experiments show that VOC absorption is favoured over H_2O, in agreement with earlier reports by Pandey et al. and Sann et al. [34, 35]. In contrast, ZIF-8 shows its strongest response [36] toward 2-butanone and the series of C_1–C_4 alcohols.

Toluene induces only a moderate change in capacitance. Although its kinetic diameter exceeds the 3.4 Å aperture of ZIF-8, framework "gate-opening" might permit uptake, as demonstrated by Khudozhitkov et al. [37] The reduced signal could originate from toluene's very low dielectric constant (2.38 vs. 1878 and its modest electronic polarizability compared to that of the other VOCs [25]). The observed differences in sensor response can arise from a combination of dielectric matching, pore-size exclusion, and guest–host interactions, as detailed in Tables 2 and Table S5.

The sensor response (ΔADC) of both inks toward all VOCs and water is shown in Figure 6e, demonstrating distinct interaction behaviors between ZIF-8 and UV ink. The results indicate that ZIF-8 ink exhibits a significantly stronger response for all VOCs except toluene, compared to UV ink. This behavior suggests that UV ink interacts more weakly with VOC molecules, likely due to the absence of microporosity compared to ZIF-8. The enhanced response of ZIF-8 ink to ketones (such as 2-butanone) and alcohols (including ethanol, methanol, 2-propanol, and 1-butanol) suggests its preferential adsorption for molecules with these functional groups. The ratios of responses to a gas across the different inks in Figure 6f provide more detailed insight into the sensor's selectivity. This highlights their relative interactions with different VOCs. The ZIF-8/UV ratio peaks for 2-butanone, whereas the reciprocal ratio is largest for toluene, indicating that the UV ink responds more strongly to it than the ZIF-8 ink.

Thus, in Figure 6f selectivity is expressed as the ratios $\Delta ADC_{\text{ZIF-8 ink}}/\Delta ADC_{\text{UV ink}}$ and $\Delta ADC_{\text{UV ink}}/\Delta ADC_{\text{ZIF-8 ink}}$ for each VOC. The high ZIF-8/UV ratios for 2-butanone and the C_1–C_4 alcohols reflect ZIF-8's stronger response to these polar VOCs, consistent with their favourable adsorption and higher dielectric constants. Conversely, the largest UV/ZIF-8 ratio is observed for toluene, confirming that the neat UV resin is more sensitive to toluene than the ZIF-8 ink. This can be attributed to the non-porous, carbon-rich polymer matrix of the UV ink, which favours sorption of non-polar aromatic molecules, whereas ZIF-8 provides microporous adsorption sites that favour smaller, more polar VOCs.

It should be emphasized that neither ZIF-8 nor the UV-curable ink is specific to a single vapour. Rather, each ink exhibits a characteristic response pattern across the VOC panel, and selectivity arises from comparing these patterns in an array context. The relatively low response of ZIF-8 to water and toluene in Figure 6e can be understood by considering both uptake and dielectric properties. ZIF-8 is strongly hydrophobic and its water uptake remains negligible up to about 80% relative humidity, as shown by the water adsorption isotherm in Figure S2c; at the ~20% RH corresponding to 6000 ppm H_2O in our experiments, only a trace amount of water is adsorbed, leading to a very small capacitance change. For toluene, the combination of limited uptake in the ~3.4–4 Å windows of ZIF-8, and the very low dielectric constant of toluene ($\varepsilon_r \approx 2.38$) results in a modest signal. In contrast, the UV-curable polymer matrix is non-porous but highly carbon-rich, and can swell and absorb toluene more effectively, which explains its larger response to toluene. Other VOCs in the test set exhibit both higher uptake in ZIF-8 and higher dielectric constants, producing the stronger signals observed in Figure 6e.

3.4.3 | Sensor Calibration for Single VOC Gas

Based on the initial multi-gas screening, we selected 2-butanone and toluene for subsequent analyzes. A typical measurement is shown in Figure 7a, where the concentration of 2-butanone is stepwise increased and decreased stepwise between 2000 and 10000 ppm and, in between, set to 0 ppm. To check the reproducibility of the measurement, each test is performed twice, as indicated by the black and red lines in the graph.

To enable quantification of gas concentrations, we first perform a calibration of the pixelated sensor for the two pure gases, 2-butanone and toluene. The response of the sensors functionalized with ZIF-8 ink and UV ink to both VOCs is characterized as outlined in the previous subsection. The results are shown in Figure 7a–f. The ΔADC values from these measurements are averaged over multiple pixels. Two tests (Test 1 and Test 2) are performed, indicated by black and red lines in Figure 7a–d, resulting in four values per gas concentration for each ink–VOC combination, which are plotted as circles in Figure 7e,f.

Three of the four datasets exhibit a linear trend and were fitted with a linear model, $\Delta ADC_{\text{ink,VOC}} = c_{\text{ink,VOC,1}} \cdot C_{\text{VOC}}$. The response of ZIF-8 to 2-butanone shows a saturation effect and was therefore fitted with a quadratic model, $\Delta ADC_{\text{ZIF,butanone}} = c_{\text{ZIF,Bu,1}} \cdot C_{\text{butanone}} + c_{\text{ZIF,Bu,2}} \cdot C^2_{\text{butanone}}$. All fits were performed using the least-squares regression method. The resulting fit parameters from this calibration procedure are summarized in Table 3, which shows in particular that the response of the ZIF-8 ink to butanone is much stronger than its response to toluene, providing selectivity.

Thus, the E-nose is calibrated for its response to two pure gases, 2-butanone and toluene. The measured ΔADC values for the two inks provide reproducible and distinguishable responses for each VOC, enabling quantitative calibration curves as shown in Figure 7e,f. These calibration results form the experimental basis for distinguishing different analytes.

To further evaluate the response of the pixelated capacitive sensor under binary gas exposure, we exposed it to mixtures of toluene and 2-butanone at equal concentrations in each cycle. The mixtures were applied stepwise from 1000 ppm of each gas up to 5000 ppm of each gas, as shown in Figure 7g. The resulting ΔADC values for both inks are plotted, with UV ink shown in black and blue lines and ZIF-8 ink in red and green lines for two

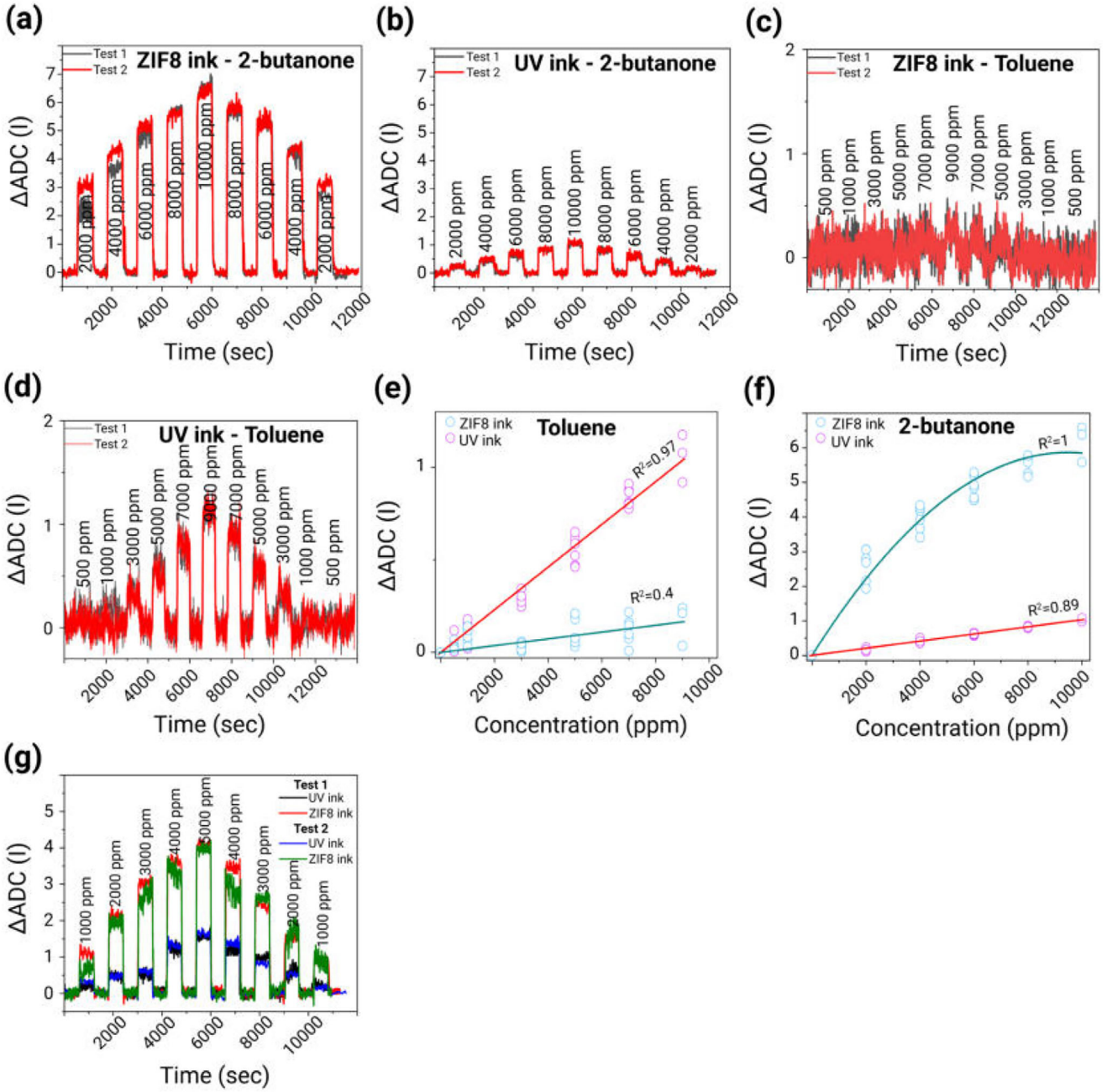

FIGURE 7 | Sensor calibration for single VOC (a) ZIF-8 ink-functionalized area response to 2-butanone, (b) UV ink-functionalized area response to 2-butanone, (c) ZIF-8 ink functionalized area response to toluene, (d) UV ink-functionalized area response to toluene. (e–f) Sensor calibration and fits: (e) Linear and quadratic fit of the sensor responses of the ZIF-8 and UV ink functionalized areas resp. to 2-butanone, (f) linear fits of the responses of the ZIF-8 and UV ink functionalized areas to toluene. (g) Sensor response of UV and ZIF-8 ink-functionalized areas to mixtures of toluene and 2-butanone gas in varying concentrations, where concentrations of both VOCs are equal, as indicated in the graph.

TABLE 3 | Extracted fitting coefficients for UV and ZIF-8 ink responses. Concentrations are given in ppm. Since ΔADC(I) is dimensionless, the linear coefficients c_1 have units of 1/ppm and the quadratic coefficient c_2 has units of 1/ppm^2.

Coefficient	Extracted value	Description (Units)
$c_{UV,To,1}$	1.153×10^{-4}	Sensitivity of UV ink to toluene (1/ppm)
$c_{UV,Bu,1}$	1.031×10^{-4}	Sensitivity of UV ink to butanone (1/ppm)
$c_{ZIF,To,1}$	1.830×10^{-5}	Sensitivity of ZIF-8 ink to toluene (1/ppm)
$c_{ZIF,Bu,1}$	1.238×10^{-3}	Linear sensitivity of ZIF-8 ink to butanone (1/ppm)
$c_{ZIF,Bu,2}$	-6.522×10^{-8}	Quadratic sensitivity of ZIF-8 ink to butanone (1/ppm^2)

independent test runs. The reproducibility between the repeated exposures confirms the stability of the sensor response to binary VOC mixtures when the two components are present at the same concentration.

Besides equimolar mixtures, we also performed a preliminary experiment in which the total VOC concentration was held constant while the relative fractions of toluene and 2-butanone were varied (see Figure S17). In this case, the ZIF-8 and UV-ink regions respond in opposite directions as the mixing ratio changes, confirming that the paired responses carry information on the composition of non-equimolar binary mixtures.

4 | Discussion

In this work, we present an E-nose with chip-integrated capacitive readout electronics that can be realized in conventional CMOS technology. Depending on the required gas sensing capabilities, the sensor area is functionalized by inkjet printing with dedicated inks. As a proof-of-principle of using the capacitive pixelated E-nose for sensing, we demonstrate the capability of the chip for detecting the response to pure gases and to binary mixtures of VOCs.

For capacitive MOF sensors, dry N_2 is an appropriate proxy for dry synthetic air with respect to VOC responses; observed differences between dry N_2 and ambient air stem primarily from humidity and background VOCs. The MOFs employed here exhibit low water uptake, limiting humidity cross-sensitivity over the ranges tested.

From these experiments, several key performance indicators can be inferred. First of all, we note from graphs like Figure 7(c) that the CMOS chip is able to distinguish very small capacitance changes of around $\Delta ADC = 0.1$, corresponding to 0.3 aF per sensor element. Noting that the simulated base capacitance of a functionalized sensor element is roughly 0.5 fF, this enables detecting changes in the effective dielectric constant of the order of 0.1%, contributing to a high sensitivity.

In our experiments, we demonstrated reproducible responses for toluene and 2-butanone in the 100–1000 ppm range. Using the rms baseline noise of the averaged ΔADC signal in dry N_2 ($rms_{noise} \approx 0.03$ ADC) and the slopes of the calibration curves in Figure 7e,f, and applying the standard 3σ criterion $LOD = 3\,rms_{noise}/S$, we estimated ink- and VOC-specific limits of detection (see in Table S6). For the most responsive combination, ZIF-8 exposed to 2-butanone, the resulting LOD is approximately 7.3×10^1 ppm. For the UV ink, the estimated LODs are about 7.8×10^2 ppm for toluene and 8.7×10^2 ppm for 2-butanone, whereas the weak response of ZIF-8 to toluene leads to a higher LOD of $\sim 4.9 \times 10^3$ ppm. These values reflect the trade-off between sensitivity and selectivity for different ink–VOC pairs and are consistent with the relative slopes observed in Figure 7e,f.

We note, however, that we foresee substantial possibilities for improving the detection limit. By engineering the electrode configuration and by improving ink composition, deposition strategy, and porosity, while also reducing sensor noise levels, it might well be possible to bring detection limits down to the 1–10 ppm range. A special point of notice is the reproducibility and fast response of the current sensor. As is seen in graphs like Figure 7c, the sensor returns rapidly (within ~100 s) and reproducibly to the initial $\Delta ADC = 0$ value after removing the VOC gas. This response time depends both on the sensor itself and on the time it takes to stabilize the gas concentration at the sensor surface after removing the VOC. The actual sensor response might even be faster than 100 s, since at the operating flow rates, the time for replacing the gas in the tubes after changing the concentration setting is of the order of a minute and thus might be limiting the response in our experiments. Since the readout electronics are very fast, we expect response times to ultimately be limited by diffusion and effusion rates of gases in the ink functionalized layers. Response times might thus be further reduced by using thinner functionalization layers, although this will probably reduce sensitivity.

The reproducibility and absence of large drifts of the sensor indicate that the gases cause no permanent chemical or physical changes in the functionalized layers. Most likely, the observed signals are therefore a result of the diffusion and effusion of the gas into the materials of which the functionalized layers consist, onto the external surfaces of the materials, but also into porous ZIF-8 and absorbed into the deposited polymer of the UV-ink. The gas that enters the bulk and/or surface of the functionalization layer, will cause a change in the effective dielectric constant. It is known [38, 39] that both toluene and 2-butanone absorb well to ZIF-8 particles. While 2-butanone has a high relative dielectric constant of approximately 18.5, toluene has a much lower dielectric constant of 2.38. The high absorption of 2-butanone in combination with its high dielectric constant can explain the high response in Figure 7h to this gas, especially of the porous ZIF-8 in the ink. The response of the sensor to toluene gas is much weaker, and surprisingly, the response of the ZIF-8 functionalized layer to toluene is weaker than the response of the layer based on UV ink in Figure 7g.

While a hypothetical explanation could be displacement of residual H_2O in ZIF-8 by toluene, this is unlikely because ZIF-8 is highly hydrophobic and the measurements were performed under dry gas conditions. Instead, the significantly higher response of the UV-ink functionalized layer suggests that toluene is absorbed into the acrylate-based polymer matrix, potentially even swelling the polymer, which would allow higher uptake compared to ZIF-8, which cannot swell. Furthermore, the UV-ink shows a stronger response to toluene than to 2-butanone, despite the latter having a higher dielectric constant. This indicates that the absorption affinity is governed by chemical interactions: the high aliphatic carbon content of the UV-ink polymer matrix favors uptake of the apolar toluene. Elemental analysis by total EDX intensity-image (97.5% carbon, see Supporting Information) supports this interpretation, consistent with preferential sorption of toluene over 2-butanone in the UV-ink layer.

This opposite response of the inks toward toluene and 2-butanone, with UV ink having the highest response to toluene and ZIF-8 ink having the highest response to 2-butanone, is beneficial for using these inks for determining the gas concentration in a mixture of the two gases. In general, for good selectivity of E-noses, it is important to find combinations of functionalization

materials that are specifically sensitive to some of the gases compared to the other gases.

The pixelated architecture with 1024 electrodes per chip is designed not only to improve signal-to-noise ratio by spatial averaging, but also to enable a high degree of chemical diversity on a single CMOS platform. In the present proof-of-principle, we use four functional layers (three MOF-based inks and one UV-curable polymer), but the same inkjet-printing approach can, in principle, be extended to many more materials. Selectivity can be modulated by combining MOFs with different pore sizes, topologies, and surface chemistries, by varying the MOF loading and composition of the polymer matrix, and by printing different inks in spatially separated microdomains on each sensor matrix. With a conservative estimate of a ∼50 μm droplet footprint, a single $\sim 400 \times 500\ \mu m^2$ matrix can host on the order of 80 distinct functionalization regions, so that using all three matrices allows for up to ∼240 different inks on one chip.

Using many partially-specific sensors in parallel increases the dimensionality of the odour fingerprint and thereby improves discrimination of complex gas mixtures, analogous to the way the mammalian olfactory system benefits from a large repertoire of broadly responsive olfactory receptors. At the same time, the time-division multiplexed readout architecture ensures that power and data-rate requirements remain manageable: all 1024 electrodes in a matrix share the same front-end and ADC and are read out sequentially, so the power consumption does not scale linearly with the number of pixels. In our implementation, the full array can be scanned every 0.3–0.5 s, which is compatible with the characteristic adsorption/desorption times of the VOCs studied.

The present study focuses on the CMOS capacitive E-nose platform itself, its functionalization, and calibration under controlled laboratory conditions. A further extension will be to upgrade the gas-mixing manifold with additional independently controlled VOC lines so that ternary and more complex mixtures (including interferents such as ethanol) can be investigated systematically and used to train multivariate models for anti-interference and decoupling of multi-component gas mixtures. In addition, translating this platform to specific application scenarios, such as greenhouse VOC monitoring or food spoilage detection, will require dedicated sampling and packaging solutions that account for dust, humidity, temperature variations, and gas-flow conditioning, including appropriate pre-filters. Designing and validating such application-specific modules, and conducting long-term field trials, fall outside the scope of this work and will be the subject of future studies, in which the chip will be integrated into complete sensor nodes and tested under realistic environmental conditions.

5 | Conclusion

We present a pixelated CMOS capacitive sensor chip that is functionalized by inkjet printing with MOF and polymer inks. The E-nose is shown to detect volatile organic compounds, with a response that can be controlled by the ink composition. A dedicated measurement methodology and analysis software are developed to process the simultaneous and continuous response of all 1024 pixel sensors and improve capacitance resolution by averaging over multiple pixels in selected functionalized regions. The sensor chip shows a stable and fast response to changes in VOC concentrations down to 100 ppm within ∼100 s under our experimental conditions. It was found that the ZIF-8 and pure UV-curable ink were the most hydrophobic compared to MIL-101(Cr) and MIL-140A. The complementary selectivity of the inks enables discrimination between 2-butanone and toluene exposure. After calibration in pure VOCs of known concentration, reproducible responses were also observed for controlled binary mixtures of the two gases. The small size, low cost, and high performance of the CMOS readout, together with the flexibility of inkjet-based functionalization, highlight the potential of this approach for further development into a multi-gas sensing platform. A remaining challenge is the synthesis and selection of inks with both high sensitivity and selectivity to targeted gases. With further optimization, the presented platform could be applied in safety monitoring, agriculture, the food industry, and robotics.

Acknowledgements

M.A.B.-M.K., P.G.S., and M.K.G. acknowledge support from the Dutch government as part of the National Growth Fund programme NXTGEN Hightech, project Agrifood 11: Greenhouse Horticulture - Digital Twin. M.A.v.d.V, C.H., and F.W. acknowledge support from the research programme Nationale Wetenschapsagenda – Onderzoek op Routes door Consortia (NWA-ORC) 2020/21, which is (partly) financed by the Dutch Research Council (NWO) under number NWA.1389.20.123. P.G.S. acknowledges funding from the European Union under the Horizon Europe Programme, Grant Agreement No. 101136388.

Conflicts of Interest

The authors declare no conflicts of interest.

Data Availability Statement

The data that support the findings of this study are available from the corresponding author upon reasonable request.

References

1. Z. Liu, M. Wang, M. Wu et al., "Volatile Organic Compounds (VOCs) from Plants: From Release to Detection," *TrAC Trends in Analytical Chemistry* 158 (2023): 116872.

2. L. Xia, Y. Liu, R. Chen, B. Weng, and Y. Zou, "Advancements in Miniaturized Infrared Spectroscopic–Based Volatile Organic Compound Sensors: A Systematic Review," *Applied Physics Reviews* 11, no. 3 (2024): 031306.

3. M. Mhanna, M. Sy, A. Elkhazraji, and A. Farooq, "A Laser–Based Sensor for Selective Detection of Benzene, Acetylene, and Carbon Dioxide in the Fingerprint Region," *Applied Physics B: Lasers and Optics* 129, no. 9 (2023): 139.

4. N. Shuaibu, C. Qin, F. Chu et al., "Traceability Tagging of Volatile Organic Compound Sources and Their Contributions to Ozone Formation in Suzhou Using Vehicle–Based Portable Single– Photon Ionization Mass Spectrometry," *Environmental Sciences Europe* 36, no. 1 (2024): 46.

5. C. Di Natale, R. Paolesse, E. Martinelli, and R. Capuano, "Solid-State Gas Sensors for Breath Analysis: A Review," *Analytica Chimica Acta* 824 (2014): 1–17.

6. O. E. Aina, N. Zine, G. Raffin, N. Jaffrezic-Renault, A. Elaissari, and A. Errachid, "Integrated Breath Analysis Technologies: Current Advances

and Future Prospects," *TrAC Trends in Analytical Chemistry* 181 (2024): 118048.

7. A. Sachan, M. Castro, and J. F. Feller, "Volatolomics for Anticipated Diagnosis of Cancers with Chemoresistive Vapour Sensors: A Review," *Chemosensors* 13, no. 1 (2025): 15.

8. Y. Li, Z. Wang, T. Zhao, H. Li, J. Jiang, and J. Ye, "Electronic Nose for the Detection and Discrimination of Volatile Organic Compounds: Application, Challenges, and Perspectives," *TrAC Trends in Analytical Chemistry* 180 (2024): 117958.

9. A. Pannone, A. Raj, H. Ravichandran et al., "Robust Chemical Analysis with Graphene Chemosensors and Machine Learning," *Nature* 634 (2024): 572–578.

10. M. Mahmud, C. Seok, X. Wu et al., "A Low-Power Wearable E-Nose System Based on a Capacitive Micromachined Ultrasonic Transducer (CMUT) Array for Indoor VOC Monitoring," *IEEE Sensors Journal* 21, no. 18 (2021): 19684–19696.

11. Y. Dang, Y. V. M. Reddy, and M. Cheffena, "Facile E-Nose Based on Single Antenna and Graphene Oxide for Sensing Volatile Organic Compound Gases with Ultrahigh Selectivity and Accuracy," *Sensors and Actuators B: Chemical* 419 (2024): 136409.

12. E. Fernandez, P. G. Saiz, N. Peřinka, S. Wuttke, and R. FernndezdeLuis, "Printed Capacitive Sensors Based on Ionic Liquid/Metal-Organic Framework Composites for Volatile Organic Compounds Detection," *Advanced Functional Materials* 31, no. 25 (2021): 2010703.

13. M. Saif, F. Jiang, S. Lo et al., "20.4 MEMS-Free 4096-Pixel CMOS E-Nose Gas-Sensor Array with Molecular-Selective Metal-Organic-Framework Sensing and In-Pixel Thermodynamic Modulation for Fast Sensor Regeneration," in *2025 IEEE International Solid-State Circuits Conference (ISSCC)*, Vol. 68, 01–03.

14. H. Darwish, C. Reig, G. Leger, G. D. P. Stanchieri, O. Aiello, and A. D. Marcellis, "A 180 nm CMOS Integrated Capacitance-to-Time Converter for Capacitive Sensing Applications," *IEEE Sensors Journal* 25, no. 19 (2025): 1–1.

15. M. Yao, W. Tang, G. Wang, B. Nath, and G. Xu, "MOF Thin Film-Coated Metal Oxide Nanowire Array: Significantly Improved Chemiresistor Sensor Performance," *Advanced Materials* 28, no. 26 (2016): 5229–5234.

16. N. Shustova, A. Cozzolino, S. Reineke, M. Baldo, and M. Dinc, "Selective Turn-On Ammonia Sensing Enabled by High-Temperature Fluorescence in Metal–Organic Frameworks with Open Metal Sites," *Journal of the American Chemical Society* 135, no. 36 (2013): 13326–13329.

17. C. Laborde, F. Pittino, H. Verhoeven et al., "Real-Time Imaging of Microparticles and Living Cells with CMOS Nanocapacitor Arrays," *Nature Nanotechnology* 10, no. 9 (2015): 791–795.

18. K. Persaud and G. Dodd, "Analysis of Discrimination Mechanisms in the Mammalian Olfactory System Using a Model Nose," *Nature* 299 (1982): 352–355.

19. Y. Pan, Y. Liu, G. Zeng, L. Zhao, and Z. Lai, "Rapid Synthesis of Zeolitic Imidazolate Framework-8 (ZIF-8) Nanocrystals in an Aqueous System," *Chemical Communications* 47, no. 7 (2011): 2071–2073.

20. J. Rouquerol, P. Llewellyn, and F. Rouquerol, "Is the BET Equation Applicable to Microporous Adsorbents?," in *Characterization of Porous Solids VII*, Studies in Surface Science and Catalysis, Vol. 160, eds. P. Llewellyn, F. Rodriguez-Reinoso, J. Rouquerol, and N. Seaton (Elsevier, 2007), 49–56.

21. J. W. Osterrieth, J. Rampersad, D. Madden et al., "How Reproducible Are Surface Areas Calculated from the BET Equation?," *Advanced Materials* 34, no. 27 (2022): 2201502.

22. J. D. Evans, V. Bon, I. Senkovska, and S. Kaskel, "A Universal Standard Archive File for Adsorption Data," *Langmuir* 37, no. 14 (2021): 4222–4226.

23. S. Zaki, M. Basyooni, M. Shaban et al., "Role of Oxygen Vacancies in Vanadium Oxide and Oxygen Functional Groups in Graphene Oxide for Room Temperature CO2 Gas Sensors," *Sensors and Actuators A: Physical* 294 (2019): 17–24.

24. C. L. Yaws, P. K. Narasimhan, and C. Gabbula, *Yaws' Handbook of Antoine Coefficients for Vapor Pressure* (Knovel Norwich, NY, 2005).

25. G. Akerlof, "Dielectric Constants of Some Organic Solvent–Water Mixtures at Various Temperatures," *Journal of the American Chemical Society* 54, no. 11 (1932): 4125–4139.

26. J. Grate and M. Abraham, "Solubility Interactions and the Design of Chemically Selective Sorbent Coatings for Chemical Sensors and Arrays," *Sensors and Actuators B: Chemical* 3, no. 2 (1991): 85–111.

27. M. Saif, F. Jiang, S.-W. Lo, et al., "20.4 MEMS-Free 4096-Pixel CMOS E-Nose Gas-Sensor Array with Molecular-Selective Metal-Organic-Framework Sensing and In-Pixel Thermodynamic Modulation for Fast Sensor Regeneration," in *2025 IEEE International Solid-State Circuits Conference (ISSCC)*, Vol. 68, 01–03.

28. F. Widdershoven, "Pixelated Capacitive Sensors (PCS) for Embedded Multi-Sensing," in *Imaging Sensors, Power Management, PLLs and Frequency Synthesizers: Advances in Analog Circuit Design 2023* (Springer, 2024), 23–35.

29. S. Najafabadi, C. Huang, K. Betlem et al., "Advancements in Inkjet Printing of Metal-and Covalent-Organic Frameworks: Process Design and Ink Optimization," *ACS Applied Materials and Interfaces* 17, no. 8 (2025): 11469–11494.

30. A. U. Ortiz, A. P. Freitas, A. Boutin, A. H. Fuchs, and F.-X. Coudert, "What Makes Zeolitic Imidazolate Frameworks Hydrophobic or Hydrophilic? The Impact of Geometry and Functionalization on Water Adsorption," *Physical Chemistry Chemical Physics* 16, no. 21 (2014): 9940–9949.

31. P. Ghosh, K. C. Kim, and R. Q. Snurr, "Modeling Water and Ammonia Adsorption in Hydrophobic Metal–Organic Frameworks: Single Components and Mixtures," *The Journal of Physical Chemistry C* 118, no. 2 (2014): 1102–1110.

32. F.-X. Coudert and co workers, "Thermodynamics of Water Adsorption in Hydrophobic Zeolitic Imidazolate Frameworks," *The Journal of Physical Chemistry C* 121 (2017): 24000–24010.

33. J. Hu and X. Yang, "Hydrophobic UV-Curable Acrylate Coatings with Low Water Uptake," *Progress in Organic Coatings* 73 (2012): 53–60.

34. S. Pandey, B. Sharmah, P. Manna et al., "Fabrication of Hydrophobic Drug-Loaded Zeolitic Imidazolate Framework-8 (ZIF-8) for Enhanced Anti-Bacterial Activity," *Journal of Molecular Structure* 1312 (2024): 138452.

35. E. Sann, Y. Pan, Z. Gao, S. Zhan, and F. Xia, "Highly Hydrophobic ZIF-8 Particles and Application for Oil-Water Separation," *Separation and Purification Technology* 206 (2018): 186–191.

36. K. Zhang, L. Zhang, and J. Jiang, "Adsorption of C1–C4 Alcohols in Zeolitic Imidazolate Framework-8: Effects of Force Fields, Atomic Charges, and Framework Flexibility," *The Journal of Physical Chemistry C* 117, no. 48 (2013): 25628–25635.

37. A. Khudozhitkov, S. Arzumanov, D. Kolokolov, and A. Stepanov, "Mobility of Aromatic Guests and Isobutane in ZIF-8 Metal–Organic Framework Studied by 2H Solid State NMR Spectroscopy," *The Journal of Physical Chemistry C* 123, no. 22 (2019): 13765–13774.

38. P. Mohammad-Gholikhan-Khalaj, M. Hasanzadeh, D. Panahi, Z. Yazdankhah, and S. F. Dehghan, "Feasibility Study on the Removal of Toluene from the Air Stream by Activated Carbon/Zeolite Imidazolate Framework Composite Material," *Journal of Environmental Chemical Engineering* 11, no. 5 (2023): 110885.

39. S. Tanaka, K. Fujita, Y. Miyake et al., "Adsorption and Diffusion Phenomena in Crystal Size Engineered ZIF-8 MOF," *The Journal of Physical Chemistry C* 119, no. 51 (2015): 28430–28439.

Supporting Information

Additional supporting information can be found online in the Supporting Information section.

Supporting File 1: aelm70386-sup-0001-SuppMat.tex

Supporting File 2: aelm70386-sup-0002-FigureS1-S15.zip

Supporting File 3: aelm70386-sup-0003-DataFiles.zip